

# Tunable shear thickening, aging, and rejuvenation in suspensions of shape-memory-endowed liquid crystalline particles

Chuqiao Chen<sup>a</sup> 🗓, Carina D. V. Martínez Narváez<sup>a</sup>, Nina Chang<sup>a</sup>, Carlos Medina Jimenez<sup>a</sup> 📵, Joseph M. Dennis<sup>b</sup>, Heinrich M. Jaeger<sup>c.d</sup> 📵, Stuart J. Rowan<sup>a,e,f,1</sup> D, and Juan J. de Pablo<sup>a,g,h,i,1</sup>

Affiliations are included on p. 8.

Edited by David Weitz, Harvard University, Cambridge, MA; received December 6, 2024; accepted May 3, 2025

The morphological features of particles, notably shape anisotropy, critically influence the rheological properties of dense suspensions, spanning both natural and engineered systems. This work explores the potential of using shape memory particles to dynamically regulate suspension fluid flow through controllable shape transformations. First, we synthesize shape-memory particles with programmable anisotropy from liquid crystal elastomers, such that the stiffness and shapes of the particles can be tuned by manipulating temperature. Our findings reveal that suspensions from such particles exhibit significant tunability in shear thickening behavior, transitioning from discontinuous shear thickening to a Newtonian-like response within a narrow temperature range of 60 °C. This capability to modulate rheological responses in situ presents an approach for addressing processing challenges in many applications where control over flow behavior is paramount. Furthermore, we also show that suspensions composed of these anisotropic particles can undergo physical aging, and evolve into a glassy state. This state can be escaped upon activation of the shape memory effect. This reversibility underscores the potential for using such materials to engineer systems that can enter or come out of kinetic arrest by leveraging internal mechanical responses to external stimuli. The insights gained here not only broaden our understanding of the interplay between particle geometry and suspension dynamics but also pave the way for leveraging ensembles of stimuli-responsive objects to precisely control collective behaviors in many-body systems.

jamming | liquid crystal | colloids | stimuli-responsive | dense suspensions

Particle shape plays an important role in numerous physical and biological systems across all length scales, ranging from molecular ordering (1, 2), colloidal self-assembly (3), tissue organization (4, 5), to the mechanics of sand dunes (6, 7). In suspensions composed of solid particles dispersed in a carrier fluid, particle shape can control how they interact, assemble, or respond to external fields (8-10). Consequently, the mechanical properties of suspensions are also sensitive to particle shape (11-13). Depending on the specific form of the underlying asymmetry, the volume fraction  $(\phi)$  of the particles, and the flow rate, the hydrodynamic and contact interactions between particles can be altered to varying extents, thereby leading to a range of peculiar phenomena such as flow-induced alignment or flow instabilities (14-16). The resulting non-Newtonian response can also lead to significant challenges in suspension processing (17).

Two types of particle shape anisotropy have been discussed in the literature, namely asphericity and angularity, as depicted in Fig. 1A (18-20). Asphericity, commonly characterized by an aspect ratio deviating from unity, endows the particles with rotational momentum in addition to translational momentum. In dilute suspensions of elongated particles, analytical expressions for the viscosity and the particles' trajectories reveal a preferred alignment along the flow direction under convective motion (21, 22). As the concentration increases to the semidilute regime, hydrodynamic interactions between particles can play a significant role, and the rotary motions between individual particles are no longer independent (23, 24). In dense suspensions with very high  $\phi$ , direct interparticle contacts can impose further constraints on the tumbling motion of the particles, leading to pronounced shear thickening. In agreement with this theoretical picture, prior experimental work has shown that dense suspensions of aspherical particles exhibit lower jamming volume fractions in both the low and high shear regimes ( $\phi_I$  and  $\phi_{SI}$ ) and are more prone to shear thickening (25, 26) (Fig. 1*B*). In addition to asphericity,

# **Significance**

Studies of colloidal suspensions have largely focused on traditional particles that exhibit isotropic mechanical properties. There is no precedent for preparing suspensions of liquid crystalline particles, where colloids can exhibit anisotropic elasticity and shape-shifting characteristics. In this work, we present results for the synthesis and rheological characterization of suspensions consisting of shape-memory particles made from liquid crystal elastomers. We demonstrate that in concentrated suspensions, temperature can be used to induce changes in material stiffness and particle shape anisotropy, thereby providing access to a wide range of flow behaviors, including a pronounced jamming transition. The findings reported here open up opportunities to leverage ensembles of stimuli-responsive objects for precise control over the collective behavior of a many-body system.

 $\label{eq:contributions: C.C., C.D.V.M.N., J.M.D., H.M.J., S.J.R., and J.J.d.P. designed research; C.C., C.D.V.M.N., N.C., and C.M.J. performed research; C.C., C.D.V.M.N., C.M. performed research; C.C., C.D.V.M.N., performed research; C.C., C.D.V.M$ C.M.J. analyzed data; and C.C., C.D.V.M.N., N.C., C.M.J., J.M.D., H.M.J., S.J.R., and J.J.d.P. wrote the paper.

The authors declare no competing interest.

This article is a PNAS Direct Submission

Copyright © 2025 the Author(s). Published by PNAS. This article is distributed under Creative Commons Attribution-NonCommercial-NoDerivatives License 4.0

<sup>1</sup>To whom correspondence may be addressed. Email: stuartrowan@uchicago.edu or jjd8110@nyu.edu.

This article contains supporting information online at https://www.pnas.org/lookup/suppl/doi:10.1073/pnas. 2425373122/-/DCSupplemental.

Published July 2, 2025.

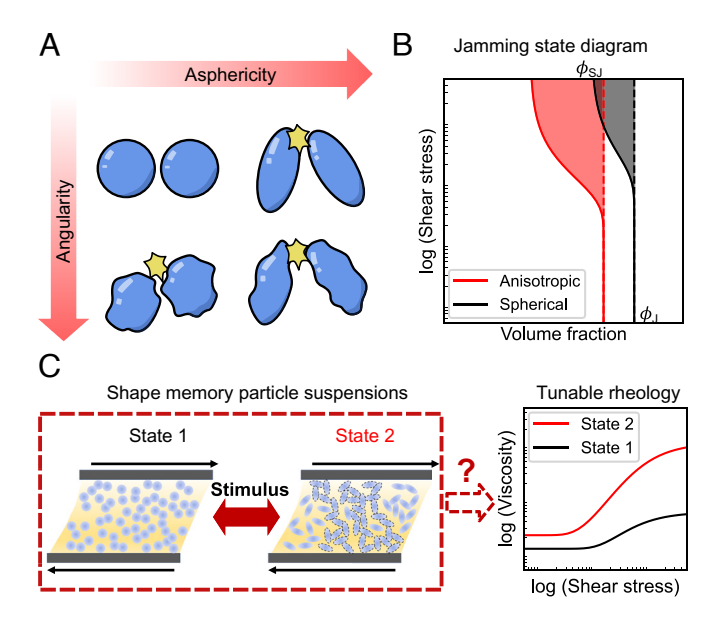


Fig. 1. Schematic for regulating suspension rheology with particle shapes. (A) Two types of shape anisotropy are illustrated. (B) Jamming state diagrams of a typical anisotropic and isotropic particle suspension are contrasted. (C) Illustration of the design of shape memory particle suspension in this work.

angularity provides another manifestation of shape anisotropy (or conversely measured as roundness) that measures deviations from a smooth spheroid (20, 27). Angularity (sometimes referred to as mesoscopic roughness) can have a large impact on particle contacts. Angular particles can present larger contact areas or mesoscale surface asperities that enhance constraints to the sliding and rolling motions of neighboring particles (28). Consequently, such suspensions display lower jamming fractions and more pronounced shear thickening compared to spherical particles at the same  $\phi$  (29-31). Many particles found in nature, such as sugar crystals, corn starch granules, and sand grains, exhibit both asphericity and angularity (32). It has been shown through shear reversal rheology that in dense suspensions of such anisotropic particles, contact forces can play a dominant role on their rheological properties under shear flow (33, 34).

While the above theoretical and experimental works underscore the effects of particle shape on the rheological properties of dense suspensions, few studies to date have thought to control suspension rheology by employing shape-shifting particles. A recent study of elastic shells that exhibit a buckling instability indicates that suspensions of spherical or collapsed shells exhibit markedly different rheological properties (35). The shapeshifting event in such a system is driven by elastic instabilities and, as such, it is spontaneous and not controllable in situ. By comparison, shape-memory particles offer an addressable platform to achieve reversible and controlled shape transformations (36, 37). Through choice of the underlying chemistry, properties such as the material stiffness, the actuation mode, and the conditions for triggering a shape change can be manipulated. One particular class of shape-memory polymer is provided by liquid crystal elastomers (LCEs), which consist of an elastic network of liquid crystalline molecules (38). The liquid crystalline ordering of the polymer chains can be disrupted or reformed by inducing the nematic to isotropic transition, leading to a large change in the dimensions of the material. Due to their simple synthesis and widely tunable properties, LCEs have found a wide range of applications in robotic and sensing devices (39-41). However, while the synthesis of LCE-based and other shape memory

colloids has been demonstrated, most studies to date have focused on the shape transformation of individual particles (42, 43). More generally, the prospect of controlling collective properties in crowded ensembles has been addressed in simulations (44), but rarely been considered in experiments, with only a few exceptions explored in different contexts (45, 46).

In this work, we explore the possibilities of shape memory materials for control of the rheological behavior of suspensions by first developing a scalable synthesis method that allows us to obtain particles with tunable degrees of anisotropy. Importantly, particle shape can be programmed through different processing steps, thereby providing access to different shapes from the same material. Particle stiffness and adhesive interactions can be regulated by modulating temperature, leading to dramatic changes of the shear thickening strength in systems with high anisotropy. We also find that solid-like materials imbued with hierarchical ordering can be obtained through aging and that a reversal to a liquid-like state can be induced by activating the shape memory response.

Our findings provide a step toward establishing that shape memory particles endowed with controllable shape transformation offer a broad avenue for regulation of the rheological properties of suspensions. From a materials science perspective, this work also introduces a design strategy for suspensions that relies on the interactions and collective behaviors of stimuliresponsive building blocks.

#### Results

Synthesis of Anisotropic Particles and Characterization of Shape Memory Properties. To access shape-memory particles capable of large changes in anisotropy, microparticles consisting of liquid crystal elastomer (LCEs) were synthesized via thiol-Michael dispersion polymerization (42). Briefly, a nematic-forming acrylate (RM257, 1) was reacted with a tetra-functional thiol crosslinker pentaerythritol tetrakis(3mercaptopropionate) (PETMP, 2) and a difunctional thiol 2,2'-(ethylenedioxy)diethanethiol (EDDET, 3) to yield microparticles with relatively narrow size dispersity (Fig. 2A). Following the reaction, the surface of the particles was modified with hydroxyl groups to promote dispersion in the carrier fluid and to prevent unwanted reactions between residual thiol and acrylate moieties on the surface (See Materials and Methods for details). Particles with four different crosslinking densities were synthesized (x-y), where y denotes the ratio between number of thiol functional groups from the tetrathiol crosslinker over all the thiol groups (Fig. 2B). High conversions of the thiol and acrylate groups were confirmed by infrared spectroscopy (SI Appendix, Fig. S1). While the particles as synthesized are spherical and exhibit a polydomain morphology when examined with polarized optical microscopy (POM) (SI Appendix, Fig. S2), upon drying under vacuum and redispersing in poly(ethylene) glycol  $(M_n = 200 \text{ g/mol})$  (PEG200), they become highly anisotropic. It is rationalized that the crowded packing and interparticle adhesion forces lead to spontaneous deformations and local alignment of the LC domains, thereby inducing the anisotropic shapes observed in our experiments (Fig. 2 B and C). Following this deformation, residual thiol and acrylates in the interior can undergo further reaction to stabilize this deformed state. We find that the small amount of residual acrylates and thiols can further react when particles are immersed in a swelling solvent over a prolonged time (See Materials and Methods for details); the anisotropic shapes are no longer stabilized in such cases and the particles only preserve a limited degree of one-way shape

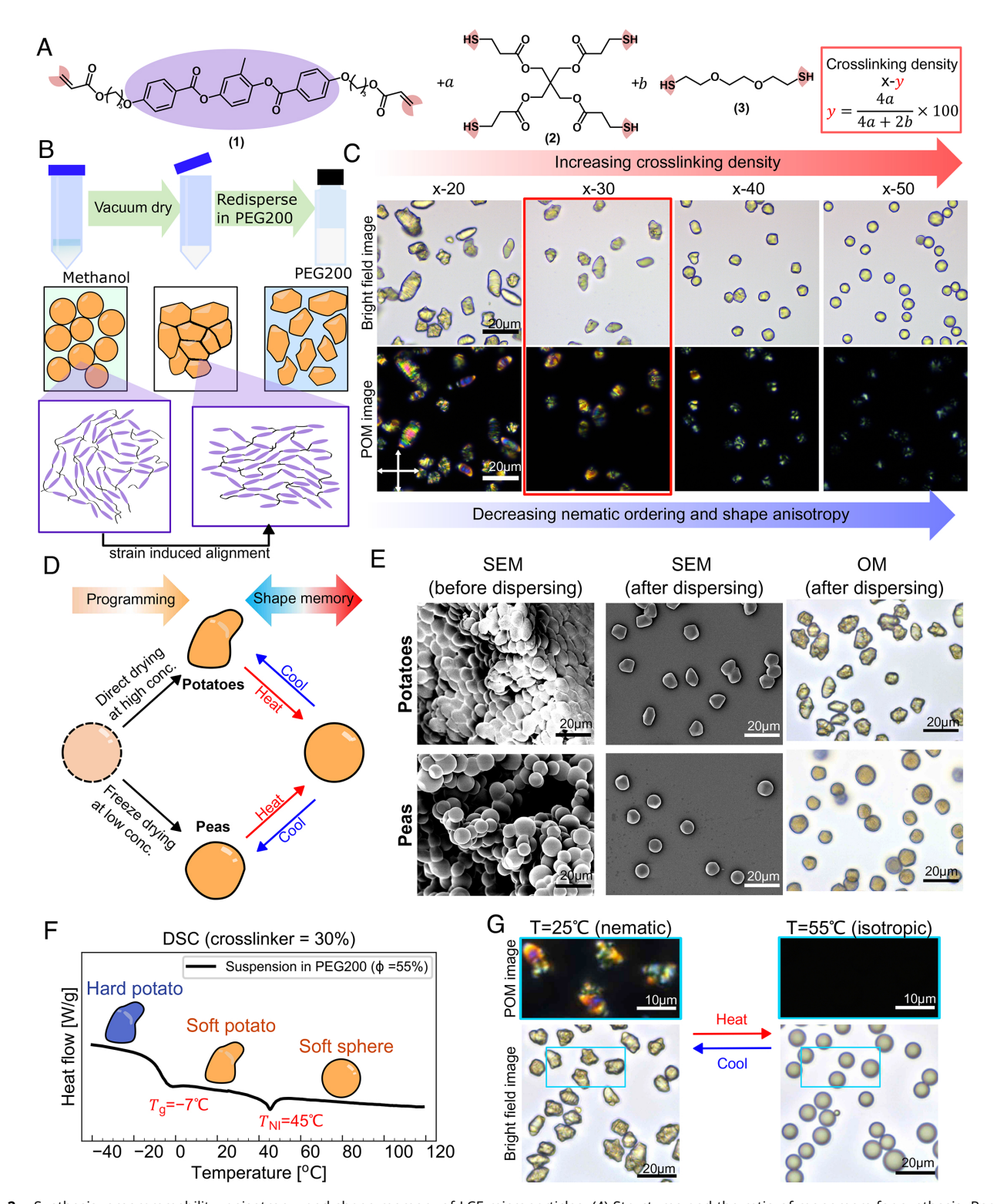


**Fig. 2.** Synthesis, programmability, anisotropy, and shape memory of LCE microparticles. (*A*) Structures and the ratio of monomers for synthesis. Reactive groups are highlighted in red. The mesogenic moiety is highlighted in purple. (*B*) Schematic of vacuum drying process and microstructural changes in LCEs. (*C*) Bright field and polarized optical microscopy (POM) images of LCE microparticles, showing decreasing anisotropy and birefringence as the crosslinking density increases. (*D*) Controlling the particle shape and thermal response by varying the drying process. (*E*) Scanning electron microscopy (SEM) images and bright field images indicate that bulk vacuum-drying yields anisotropic LCE microparticles with a potato shape, whereas pea-like particles are obtained via freeze-drying in water. (*F*) DSC curves of normalized heat flow as a function of temperature for 30% crosslinked particles suspended in PEG200 show  $T_{\rm N}$  around  $T_{\rm N}$  around 45 °C. (*G*) Shape memory response of the x-30 particles suspended in PEG200. Temperature increase above  $T_{\rm N}$  disrupts the nematic ordering and triggers a change to a spherical shape with reversibility upon cooling below  $T_{\rm N}$ .

memory (*SI Appendix*, Fig. S2). Importantly, the amount of shape anisotropy can be tailored by varying the crosslinking density of the particles (Fig. 2C). From the bright field and POM images

of the LCE particles, it can be appreciated that increasing the crosslinking density leads to decreased anisotropy and nematic ordering, but creates more monodisperse particles (Fig. 2C

and SI Appendix, Fig. S3). To access high anisotropy while maintaining relatively a narrow size distribution, an intermediate crosslinking density x-30 is chosen for the remainder of this study.

To examine whether the anisotropic shapes are in fact driven by the interparticle contacts that are prevalent in the crowded environment that arises from the drying process, one can test whether suppressing such contacts can lead to more isotropic shapes. Indeed, when the same x-30 particles are freeze-dried from dilute (3 wt%) suspensions in water, we arrive at nearly spherical particles with only a few flat facets. To distinguish the two shapes, we refer to the more anisotropic particles as "potatoes" and to the less anisotropic particles as "peas" (Fig. 2D; See SI Appendix, Fig. S3 for aspect ratio distributions and SI Appendix, Figs. S4 and S5 for additional POM and confocal images). Scanning electron microscopy (SEM) images reveal that direct vacuum drying yields close-packed particles with large deformations (Fig. 2E; See SI Appendix, Fig. S4 for comparison between POM images of pea- and potato-shaped particles). In contrast, the freeze-drying process leads to a sparser structure characterized by fewer contacts and less severe deformations. To create suspensions, upon dispersing the particles in ethanol (for SEM images) or PEG200 (for OM and rheology), the potato or pea shapes are maintained (Fig. 2*E*). Note that the surfaces of the individual particles appear smooth on the SEM images, suggesting that the particle textures that appear on the OM images more likely originate from the light scattering from the different LC domains. PEG200 is selected as the carrier fluid for the rheological studies for the following reasons: 1) It does not lead to pronounced swelling of the particles, so the anisotropic shapes can be maintained. (See *SI Appendix*, Fig. S4 for the measurement of swelling). 2) It has a high boiling point and prevents evaporation at elevated temperatures during rheological measurements. 3) PEG200 interacts favorably with hydroxyl-functionalized particles, and the particles remain well-dispersed at intermediate time scales (47).

To probe the underlying thermal transitions, differential scanning calorimetry (DSC) was performed for both the dry particles and the dense suspension ( $\phi = 55\%$ ). The glass transition temperature (Tg) and the nematic to isotropic transition temperature  $(T_{NI})$  in the suspensions are -7 °C and 45 °C, respectively. Compared to the dry particles,  $T_{\rm g}$  is reduced by ~15 °C, revealing the plasticization effect by the carrier fluid (48, 49). Our measurements confirm that the  $T_{\rm g}$  and  $T_{\rm NI}$  of the peas and potatoes are identical, implying similar thermomechanical properties (SI Appendix, Fig. S4). The simple strategy of programming the particles' shape via the drying conditions allows us to independently assess the effect of shape anisotropy without incurring unwanted changes in the mechanical properties of the particles.

After heating and cooling the suspension (diluted to ~1 vol%) under POM, the deformed particles fully transition to spherical shapes around 55 °C and the birefringence colors disappear (Fig. 2). The onset of the transition is around 40 °C, consistent with the DSC measurements. For the highly irregular shapes of the potato particles, repeated heating and cooling reveals that full recovery in shape is attained once the sample is cooled to room temperature (Movies S1–S4). In other words, the nematic-isotropic transition provides a robust mechanism to consistently access different shapes by tuning the temperature of the suspension.

Note that, in addition to altering particle shape, changes of temperature can simultaneously modify the stiffness of the

particles, which can influence considerably the rheology of the suspension (48, 49). The thermomechanical properties were evaluated by performing oscillatory rheology on a monolithic film analog with identical chemical composition as x-30. Fig. 3A shows the storage and loss moduli (G' and G'') for a film that was equilibrated in PEG200 for two weeks (See SI Appendix, Fig. S5 for the data of the dry film) For  $T < T_g$ , the storage shear modulus (G') of the glassy particles is around  $5 \times 10^8$  Pa. Above the  $T_{\rm g}$ , the particles are rubbery, with average G' around  $1 \times 10^6$ Pa in the nematic state ( $T_{\rm g} < T < T_{\rm NI}$ ), and 2 × 10<sup>5</sup> Pa in the isotropic state  $T > T_{\rm NI}$ . Notably, tensile testing shows that the LCE material exhibits semisoft elasticity and the stress to induce alignment is around 47 kPa in x-30 (SI Appendix, Fig. S5). While this stress is at least 10 to  $30 \times$  larger than the typical shear stress generated by fluid flow in the suspension, it can be accessed from the interparticle adhesion forces during the drying process (See *SI Appendix* for details).

Shear Rheology of Dense Suspensions. Steady shear viscosity measurements were performed on LCE microparticle suspensions  $(\phi = 55\%)$  as a function of shear stress for different temperatures ranging from -10 °C to 50 °C, spanning values below  $T_{\rm g}$  and temperatures above  $T_{NI}$ . To account for the variation of the carrier fluid viscosity( $\eta_0$ ) with temperature, the relative viscosity  $\eta_r$  is computed as  $\eta_r = \eta(T)/\eta_0(T)$  as shown in Fig. 3B (See SI Appendix, Fig. S9 for measurements of  $\eta_0(T)$  and additional rheology data). The strength of the shear thickening response decreases dramatically with increasing temperature. Discontinuous shear thickening (DST) is observed for 5 °C and -10 °C when the particles are below or around their  $T_g$ . As Tincreases above the  $T_{\rm g}$  of the particles, flow curves at 20  $^{\circ}{\rm C}$  and 35 °C display a continuous shear thickening (CST) response (See SI Appendix, Fig. S10 for G' and G'' determined from oscillatory measurement). In contrast, a Newtonian-like response is observed at 50 °C. The parameter  $\beta$ , obtained by fitting a power law to viscosity-stress plots ( $\eta \propto \tau^{\beta}$ ), is used to quantify the maximal strength of shear thickening (Fig. 3C; See Materials and Methods for details). Fig. 3B summarizes the  $\beta$  dependence as a function of T. Remarkably, over a relatively small temperature range, LCE microparticle suspensions with a fixed volume fraction ( $\phi$ = 55%) exhibit pronounced  $\beta$  changes from  $\beta > 1$  to  $\beta \approx 0.2$ , i.e. from DST to nearly Newtonian response. In comparison, typical dense suspensions of stiff nonresponsive particles (e.g. silica particle suspensions) show minimal temperature variations in  $\beta$  for a fixed volume fraction (50, 51). For instance, to access a similar  $\beta$  range, the corresponding volume fraction would have to be varied from 30% to 57 to 58% in silica particle suspensions (Fig. 3E) (50). In prior work, we showed that accessing the polymer glass transition provides a strategy to tune the non-Newtonian response in situ of a suspension of spherical particles from mild to strong shear thickening. In the absence of shape change, an increase from  $\beta = 0.6$  to  $\beta = 0.9$ (48) was observed as temperature was varied around  $T_g$ , which was attributed to significant changes in stiffness and interparticle adhesion (48). In contrast to that earlier system, which relied only on the  $T_g$  transition, the thermal response of LCE microparticle suspensions is much more pronounced (from  $\beta > 1$  to  $\beta \approx 0.2$ ), a feature that we attribute to the combined effects of shape and stiffness changes.

The shear thickening behavior of "pea" suspensions is less pronounced than that of the potato suspensions for all temperatures below  $T_{\rm NI}$  (Fig. 3D and SI Appendix, Fig. S11). The difference

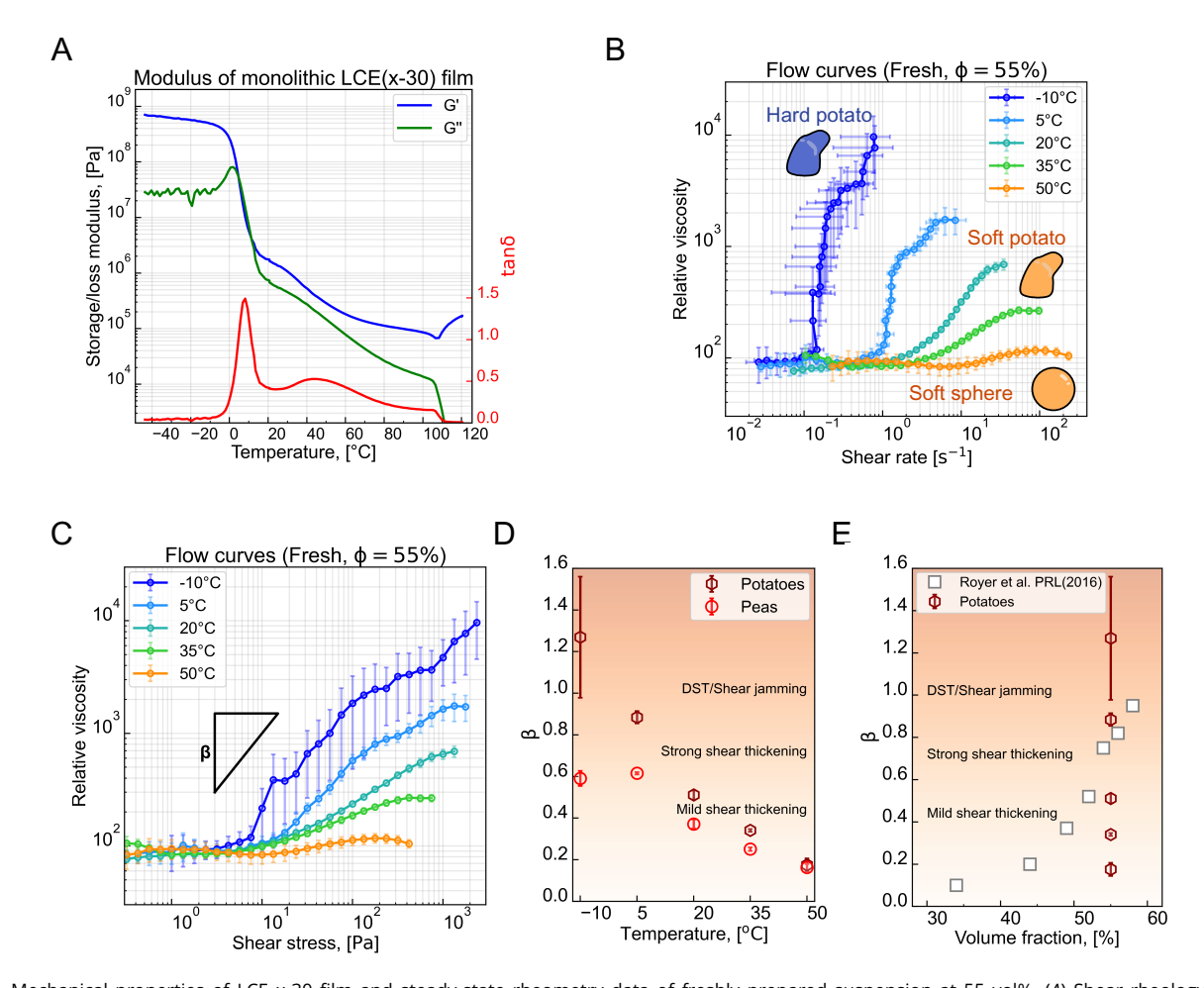


**Fig. 3.** Mechanical properties of LCE x-30 film and steady-state rheometry data of freshly prepared suspension at 55 vol%. (*A*) Shear rheology dynamic temperature sweeps on solid LCE film after soaking in PEG200 for 2 wk. (temperature ramp rate = 3 °C/min, frequency = 1 Hz, and parallel plate geometry) showing storage moduli (blue line), loss moduli (green line) and tan delta (red line) of the LCE (See *Sl Appendix*, Fig. S8 for the data of dry film). (*B* and *C*) Steady shear viscosity of LCE microparticle suspensions ( $\phi$  = 55%) normalized with solvent viscosity shows temperature-dependent strength of shear thickening. (*C*) The data in (*B*) are replotted as a function of shear stress. A reference slope of 1 that corresponds to the onset of DST is shown with a black triangle in (*C*). (*D*) The strength of shear thickening ( $\beta$ ) as a function of temperature for  $\phi$  = 55% LCE suspensions decreases with temperature spanning from DST to CST values. Potato-like particles exhibit a remarkably higher  $\beta$  at low temperatures compared to pea-like shapes. (*E*) A comparison of typical  $\beta$  as a function of volume fraction from literature with values shown in (*C*) reflects the high tunable strength of shear thickening LCE suspensions, which in regular systems can only be achieved by increasing particle volume fraction. Data for silica particle suspension are extracted from ref. 50.

in  $\beta$  value is highest when the particles are below or around  $T_{\rm g}$  (dark and light blue curves at  $T=-10\,^{\circ}{\rm C}$  and 5 °C). This result is consistent with the view that more anisotropic shapes typically exacerbate shear thickening in suspensions of stiff particles. At 50 °C (above  $T_{\rm NI}$ ), both the peas and the potatoes transition to soft spheres and the  $\beta$  parameters are statistically identical. In between  $T_{\rm g}$  and  $T_{\rm NI}$ , the particles are simultaneously soft and anisotropic. While  $\beta$  for "potato" suspensions is larger than for the "pea" suspensions for all temperatures below  $T_{\rm NI}$ , the difference for "soft potato" suspension is significantly reduced from that observed in the "hard potato" regime. This result, together with the previous observation that soft potatoes only show mild shear thickening highlights the synergistic effects of stiffness and shape anisotropy in generating effective constraints on particle motions.

**Physical Aging and Rejuvenation.** The steady-state shear rates in these shear thickening suspensions at a given shear stress  $(\tau)$  can be reached within 25 s, with nearly no hysteresis observed in the ramp-up and ramp-down curves (*SI Appendix*, Fig. S11).

While the suspension remains stable over the first 3 d with no perceivable changes in the rheological curves (see SI Appendix, Fig. S12 for oscillatory data as a function of days), substantial aging is observed after 12 d and the suspension evolves to display a solid-like texture. (Fig. 4A). Oscillatory shear rheology was performed in these aged samples (Fig. 4B), and the flow curves under steady shear are displayed in Fig. 4C. The oscillatory shear measurement at 20 °C reveals a solid-like behavior, with G' larger than G'' up to a yield stress around  $100 \pm 30$  Pa. Steady shear measurements show that at the low temperatures corresponding to the "hard potato" state, the material behaves as a solid and does not show significant yielding, indicating that the dynamics of the particles are essentially locked in a glassy state of high rigidity (52). As temperature increases to 20 °C and 35 °C, a visible yield stress is observed, implying that the stress-bearing structures can be partially destroyed by shear. However, the ramp down curve still presents a yield stress of about 80 Pa, rather than regaining the shear thickening behavior as in the fresh suspensions (SI Appendix, Fig. S11). In other words, a maximal shear stress of about 800 Pa is insufficient to break down all the clusters

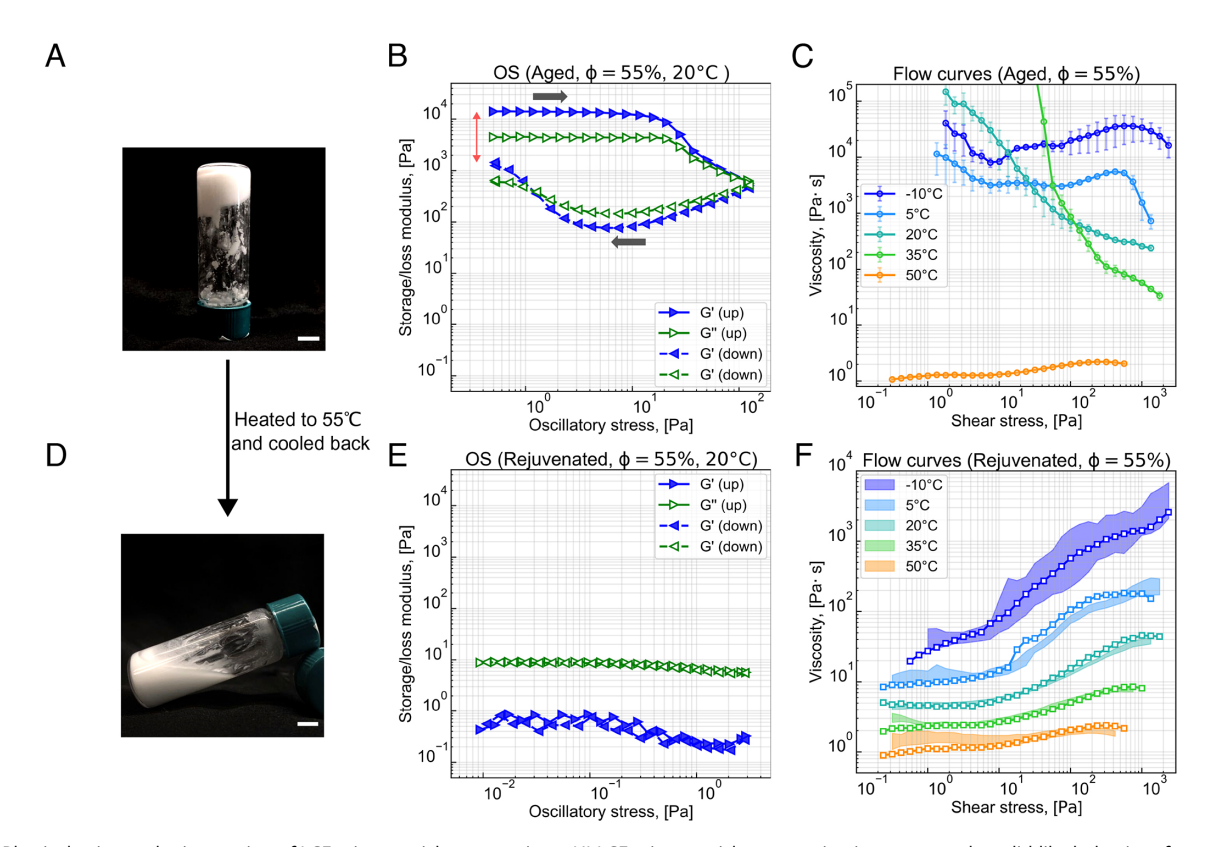


**Fig. 4.** Physical aging and rejuvenation of LCE microparticle suspensions. (A) LCE microparticle suspension images reveal a solid-like behavior after some time under quiescent conditions. (B) Oscillatory shear rheology for the aged sample. The gray arrow corresponds to data acquired on increasing or decreasing shear stress  $(\tau)$ . The red double arrow indicates hysteresis in G'. (C) Steady shear viscosity as a function of shear stress for aged samples shows signatures of yielding except for the flow curve at 50 °C. (D) The aged LCE suspension flows when the sample is heated above  $T_{NI}$  and cooled back. (E) Oscillatory shear rheology for the rejuvenated sample. (F) Flow curves of LCE microparticles after heating to 55 °C and cooled back show good agreement with flow curves for fresh samples shown in Fig. 3C.

formed. By contrast, flow curves taken above the  $T_{\rm NI}$  (50 °C) display no yielding and show a Newtonian-like response, similar to that observed in the fresh state. These findings provide ample motivation to explore whether the rheology of the suspensions can be restored by triggering the shape memory response through heat.

Upon heating to 55 °C and cooling, the suspension regains its fluid-like property, showing G' < G'' at all resolvable oscillatory stresses (Fig. 4D). Contrasted to the ramp down curve of the aged sample (Fig. 4B), the G' in thermally rejuvenated sample is about two orders of magnitude lower, implying that temperature triggers a more significant change in the suspension microstructure than pure oscillatory shear. The flow curves overlaid with the fresh sample (in shaded region) are shown in Fig. 4F. While some small differences are seen between the fresh state and the rejuvenated state, the "rejuvenated" suspension displays shear thickening behavior as opposed to the thinning behavior observed in the aged samples, implying that the microstructure of the fresh suspension is restored.

**Reconfiguration of Microstructure.** The emergence of a large yield stress implies that the particles undergo agglomeration to form a percolated particle network that provides elasticity (52, 53). To understand the microscopic mechanisms, optical microscopy was performed on the aged samples. The suspension was diluted to 5% to facilitate visualization. Despite the sample experiencing unavoidable flow during the preparation of the microscopy sample, large agglomerates of particles still persist (Fig. 5A). Upon heating, the particles transition to spherical

shapes. Strikingly, this shape-memory response of individual particles is accompanied by the dissolution of the large clusters, implying that a cooperative mechanism is involved in the rejuvenation of suspensions (Movie S5). This observation is consistent with a recent study on the collective behaviors of assemblies of shape-changing strips (46). It was reported that the strips reversibly form clusters and break up upon transitioning from straight and curled shapes, demonstrating that the collective structure formed from multiple interacting shape-shifting objects can display cooperative reordering through the shape change of the individual components. In our studies, the particles interact via adhesive interactions at contacts. After  $T_{NI}$  was reached, the suspension was cooled to room temperature, where the shapes of the individual particles were recovered. However, the agglomerated structure was not recovered, and the particles remained well-dispersed after cooling (Movie S6).

The mechanism of aging and the reconfiguration triggered by shape change is illustrated in Fig. 5*B*. Initially, the anisotropic particles are well dispersed (state 1). However, because LCEs can develop strong adhesive interactions upon contact, agglomerates are developed over time. To probe the strength of adhesion experimentally, we performed adhesion measurements on a x-30 film in the dry state (*SI Appendix*, Fig. S13). The measurement was conducted with a spherical stainless steel probe (diameter R=2.5 mm). Our results show that the adhesion force is negligible at -10 °C and 5 °C, and increases dramatically as the material becomes deformable above  $T_{\rm g}$  (*SI Appendix*, Fig. S13). In the nematic state, the surface energy, estimated by  $\gamma=F_{ad}/4\pi R$ , displays a peak. Notably, the stress generated

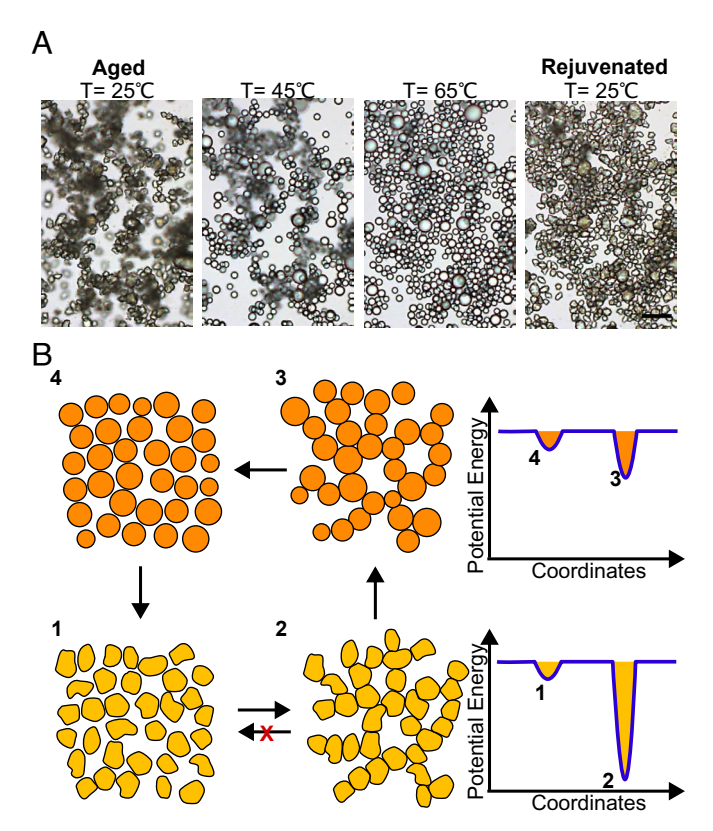


**Fig. 5.** Mechanism of microstructure reconfiguration. (*A*) OM images captured on heating and cooling of aged suspensions shows the reconfiguration of the microstructure near  $T_{\rm NI}$ . (Scale bar: 40  $\mu$ m.) (*B*) Schematics of the potential energy landscapes and the corresponding microstructures.

from this adhesion force is around  $P = \gamma/\pi R \approx 50 \sim 200$  kPa, comparable to the soft elastic plateau 47 kPa determined from the tensile tests (*SI Appendix*, Fig. S8). Therefore, it is possible that the LC domains can realign at the interface of the particle contacts, leading to stronger adhesion. The effect of enhanced adhesion with longer contacting times has been observed in the LCE literature (54), and in our systems it can facilitate physical aging through formation of more resilient agglomerates. Hence, the aged microstructure is trapped in a deep energy well (state 2), consistent with the observations that in our system the aging is irreversible by moderate mechanical shear.

As temperature is increased above  $T_{NI}$ ,  $\gamma$  decreases (54, 55) (SI Appendix, Fig. S13). Furthermore, the effective contact area also decreases as the faceted shapes become spherical above  $T_{\rm NI}$ (Fig. 5B state  $2 \rightarrow$  state 3). While the quantitative change in effective contact area is difficult to estimate (due to the complexity of the shapes and orientation distributions), literature studies on ellipsoidal and angular particles suggest that anisotropy can increase contact areas (56, 57). This combined change in shape and surface energy therefore causes the suspension to present a shallower energy well (state 3) in the clustered organization above  $T_{\rm NI}$  than in the nematic state (state 2). Second, the particles can exert forces on each other during actuation. The stress is estimated to be on the order of the particle stiffness  $\sim 10^6 Pa$  (58, 59). This stress is much larger than the stress accessible through shear rheology ( $\sim 10^3$  Pa), and offers an additional driving force beyond thermal fluctuations to overcome the adhesive forces, thereby disrupting the microstructure. Consequently, the agglomerates break down at T=65 °C as depicted in state 4 and the welldispersed fresh state (state 1) can be recovered upon cooling.

It is important to note that this phenomenon is different from reversible gelation, which has been reported in octadecyl-coated silica rods (60). The system introduced in this work presents two meta-stable trapped states at ambient conditions (61), which exhibit distinct rheological properties, and with the capacity to interconvert via slow aging or thermal rejuvenation.

## **Discussion**

The results reported here demonstrate that shape memory particles from liquid crystal elastomers give rise to a wide range of rheological behaviors within a single materials system. Two important properties are worth highlighting again. First, the shear thickening strength displays unprecedentedly strong in situ tunability, allowing access to discontinuous shear thickening or Newtonian-like rheology at the same volume fraction over a change of temperature of around 60 °C. This feature provides on-demand suppression of flow thickening and may present a route for overcoming challenges in the 3D printing of polymerparticle composites, for example, where thickening and jamming can be detrimental (62, 63). From a fundamental perspective, it is important to note that the effects of particle anisotropy are much more pronounced in stiff particles than in soft ones, implying that the effective constraints depend simultaneously on the geometry and the mechanical properties of the material.

We find that suspensions of particles with short-ranged sticky interactions undergo slow aging into a granular glass, which can be reversed by triggering the shape memory response. Aided by the actuation force and the decreased adhesion above  $T_{\rm NI}$ , the agglomerates formed over time can be disrupted, leading to instant rejuvenation of the rheological properties of the suspension. Taken together, our results show that in crowded environments, the dynamic changes of individual objects can lead to collective reconfiguration, allowing an otherwise kinetically arrested system to access different microstates. We hope these findings will motivate design of new classes of synthetic material systems based on the collective actions of interacting stimuli-responsive objects.

#### **Materials and Methods**

**Materials.** Reactive mesogen 257 (1,4-bis-[4-(3-Acryloyloxypropyloxy)benzoyloxy]-2-methylbenzene) (RM257) was purchased from Evonik (formerly Wilshire Technologies). Pentaerythritol tetrakis(3-mercaptopropionate) (PETMP, 95%), 2,2'-(Ethylenedioxy)diethanethiol (EDDET) (95%), triethylamine (99%), dipropylamine (99%), polyvinylpyrrolidone (average molecular weight 40 kg/mol) were purchased from Sigma Aldrich and used as received.

### Methods.

# Synthesis of LCE particles.

**Reaction.** For crosslinking density studies, the particles were synthesized at 20 mL scale. For example, x-30 particles were synthesized via dispersion polymerization following literature procedures. Monomers 0.400 g (0.68 mmol) of RM257 and 0.050 g (0.10 mmol) of PETMP and 0.087 g (0.48 mmol) of EDDET and 0.005 g of radical scavenger BHT were dissolved in 12 mL methoxyethanol by sonication and heating in a water bath at 50 °C. 0.2 g of PVP was dissolved in 8 mL ethanol and transferred to the reaction flask. The mixture of monomers and surfactant was stirred at 450 rpm using a magnetic stir. The reaction was started by adding in the base catalyst triethylamine (0.038 g, 7.2 wt% relative to monomers) which was diluted by  $5\times$  beforehand in ethanol by volume. The reaction was carried out for 20 h at ambient conditions. To obtain particles for suspension rheology, the reaction was scaled up to 300 mL scale with a mechanical stirrer to produce around 6.5 g particles.

**Functionalization.** To prevent surface residual groups of thiols and acrylates to react over time, monofunctional thiol and acrylates were added to end-cap

Table 1. Mass of reagents (in grams) for reactions at 20 mL scale

Chemicals/species	x-20	x-30	x-40	x-50
PETMP	0.033	0.050	0.066	0.083
EDDET	0.100	0.087	0.074	0.062
RM257	0.400	0.400	0.400	0.400

these groups. First, 0.029~g (0.272~mmol) of mercaptodiol were diluted with 1 mL of ethanol and added to the reaction mixture. Base catalyst dipropylamine (0.038~g, 7.2~wt% relative to monomers) was added to promote the reaction. After two hours, 0.063~g (0.544~mmol) of hydroxyethylacrylate were added to react with residual thiols and left for another two hours.

**Work up.** The base was neutralized by 1M HCl aqueous solution prior to centrifugation. The dispersion was centrifuged at 1,750 m/s<sup>2</sup> for 6 min and the supernatant was thrown away. To remove the surfactants and catalyst, the particles were washed in methanol at a concentration of around 0.04 g/mL under sonication and vortexing, followed by centrifugation. This step is repeated for 3×.

Synthesis of x-20, x-40, and x-50 particles follow similar procedures. The amount of the monomers were adjusted to keep the stoichiometric ratio of thiol to vinyl functional groups as 1:1. The amount of the chemicals are shown in the Table 1.

To produce potato-shaped particles, the suspension in methanol is centrifuged and the supernatant is discarded. The particles are dried under 1 torr of vacuum for 24 h. To produce pea-shaped particles, the solvent is substituted to water and the density was controlled to be around 2.5 wt%. The suspension is quickly frozen in liquid nitrogen and dried in a lyophilizer for 4 d.

To produce particles that are not capable of second-step crosslinking during drying, the surface functionalization step is carried out in tetrahydrofuran (THF) such that the particles are swollen during the reaction. The amounts of mercaptodiol, hydroxyethyl acrylate, and dipropylamine are increased by  $5\times$ . In addition, each functionalization step was carried out overnight to promote conversion

**Suspension preparation.** To make the suspension, the volume fraction is converted to the weight fraction based on the density of LCE particles and the PEG200 carrier fluid. The mixture of particle chunks and the carrier fluid is stirred vigorously for 20 min and sonicated for 25 min. The sample is allowed to equilibrate for 12 to 20 h to obtain the sample in the "fresh state."

**Synthesis of LCE analog films.** Monomers are dissolved in toluene at 50 wt/vol%. Dipropylamine (2 wt% relative to monomers) were added to initiate the reaction. The monomer solution is mixed and quickly injected to a 25 mm  $\times$  60 mm  $\times$  1 mm mold and put in a toluene solvent chamber. After 12 h, the film is sequentially washed by swelling and deswelling THF, methanol, THF, methanol to remove the remainder catalyst. The film is dried in a vacuum oven at 5 torr 60 °C overnight.

*FT-IR spectra*. Shimadzu IRTracer-100 FT-IR with ATR diamond was used to characterize the LCE particles. Reduction of the thiol peak near 2,550 cm<sup>-1</sup> and the alkene peak near 800 cm<sup>-1</sup> were used to monitor the reaction.

**Polarized optical microscopy.** Leica DM2700P polarized optical microscope equipped with MC170 HD5 camera was used to obtain POM images of the particles. Images were acquired with a  $50 \times$  or  $20 \times$  objective under transmission mode. To control temperature during measurement, INSTEC MK2000 hot and cold stage was used. Heating and cooling rates of 3 °C/min were used for typically shape memory studies (64).

**Confocal microscopy.** 2D confocal image of LCE particles was captured using a SoRa Subdiffraction Marianas Spinning Disk Confocal Microscope equipped with a Zeiss inverted microscope with an automated stage and a piezo-controlled fine Z stage. Nile Red was used to stain the LCE particles and make them fluorescent. A 561 nm solid-state laser was used for excitation, with fluorescence emission collected through a 600/50 nm bandpass filter. A 40× oil-immersion objective (NA 1.3) was used for imaging. The Yokogawa-type spinning disk, equipped with 50 upmu m pinholes, allowed for optical sectioning with minimal phototoxicity. Images were recorded with a scientific CMOS camera that has a pixel size of 0.2642 upmu m and a resolution of 1,192 × 1,200 pixels. The images were then processed and analyzed in FIJI (ImageJ) (65).

**Scanning electron microscopy.** The particles were solvent casted with methanol on silicon wafers and dried in air. Before the SEM analysis, the particles were sputter coated with an 8 nm film of Pt/Pd metal to enhance electron conductivity. The images were recorded on a Merlin SEM (Carl Zeiss) at a voltage 1.5 kV using Inlens detectors and each image was averaged between 8 to 15 images. Particle sizes were analyzed with ImageJ.

**DSC measurements.** DSC was performed with Discovery 2500 Differential Scanning Calorimeter. 5 to 10 mg of sample were prepared in aluminum hermetic pans from TA. Typical tests consist of a heat-cool-heat cycle (—40 °C to 120 °C) at a rate of 5 °C/min. The data from the second heating cycle were presented.

**Density determination.** Density of the LCE particles was determined at 25 °C by employing an Anton Paar Ultra5000 gas pycnometer using UHP He gas. The density of carrier fluid PEG200 was determined by a densimeter (DMA 4500 M, Anton Paar)

Shear rheometry measurements. Rheological characterization was performed using a Discovery Hybrid Rheometer 30 (DHR) (TA Instruments). For measurements above 5 °C, temperature was controlled by a peltier plate. For measurements at -10 °C, forced convection oven (20 °C to 500 °C) attached to an Air Chiller System (-120 °C to 20 °C) was employed. All the rheometry data were acquired with 20 mm sand-blasted plates to prevent slip. Change of the gap size due to temperature was calibrated beforehand. The suspension was loaded to the rheometer and extra fluid was trimmed at a typical gap size of 220  $\mu m$ . The measurement gap size was typically maintained at 200  $\mu m$ throughout the measurement. Temperature was equilibrated for 10 min before each measurement followed by a preshearing step at a stress around  $2\times$  of the onset shear stress for 2 min. At each stress value, the fluid was equilibrated for a minimum of 25 s and averaged over 15 s. For measuring the viscosity of PEG200, the temperature ramp experiments were carried out at a shear rate of  $50 \,\mathrm{s}^{-1}$ . The temperature was ramped at 1 °C/min from -20 °C to 75 °C. Data from -15 °C to 55 °C was fitted with a Vogel-Fulcher-Tammann-Hesse (VFTH) equation.

To compute  $\beta$  for each measurement, the rolling slope is extracted from linear regression of  $\log \eta$  vs.  $\log(Shearstress)$  between 5 data points. The maximum of this rolling average is designated as  $\beta$ . At least three trials are performed at each temperature and the mean and error are reported.

**Small amplitude oscillatory shear (SAOS) measurements of dense suspensions.** Rheological characterization was performed using an Discovery Hybrid Rheometer 30 (DHR) (TA Instruments).

**Modulus measurement of the solid films.** Tests were conducted on a DHR rheometer (TA Instruments) equipped with Forced Convection Oven (20 °C to 500 °C) attached to an Air Chiller System (-120 °C to 20 °C). The temperature was ramped at 1.5 °C/min and the oscillatory frequency used was 1 Hz. For measuring the plasticized films, the films were soaked in their respective carrier fluid at 20 °C above  $T_g$  for 10 d and the measurement was done while immersed in the carrier fluid.

**Tensile tests.** All tensile test data were collected using a Zwick-Roell zwickiLine Z0.5. The samples were prepared by cutting rectangular strips (approx. 5 mm  $\times$  0.5 mm  $\times$  15 mm) from x-30 films. The samples were uniaxially stretched at varying rate of 0.05%/s to 2%/s to 300 kPa, held at 300 kPa for 180 s and released.

**Data, Materials, and Software Availability.** All study data are included in the article and/or supporting information.

**ACKNOWLEDGMENTS.** This work was primarily supported by the University of Chicago Materials Research Science and Engineering Center, which is funded by NSF under Award No. DMR-2011854. This work was also supported by Army Research Laboratory Cooperative Agreement, W911NF-20-2-0044 (J.M.D.).

Author affiliations: <sup>a</sup> Pritzker School of Molecular Engineering, University of Chicago, Chicago, IL 60637; <sup>b</sup>Army Research Laboratory, Aberdeen Proving Ground, MD 21005; <sup>c</sup>Department of Physics, University of Chicago, Chicago, IL 60637; <sup>d</sup>James Franck Institute, University of Chicago, Chicago, IL 60637; <sup>e</sup>Department of Chemistry, University of Chicago, Chicago, IL 60637; <sup>f</sup>Center for Molecular Engineering, Argonne National Laboratory, Lemont, IL 60439; <sup>g</sup>Department of Chemical and Biomolecular Engineering, Tandon School of Engineering, New York University, Brooklyn NY 11201; <sup>h</sup>Department of Computer Science, Courant Institute of Mathematical Sciences, New York University, NY 10012; and <sup>l</sup>Department of Physics, New York University, NY 10012

- M. D. Ediger, J. de Pablo, L. Yu, Anisotropic vapor-deposited glasses: Hybrid organic solids. Acc. Chem. Res. 52, 407-414 (2019).
- J. F. Woods et al., Shape-assisted self-assembly. Nat. Commun. 13, 3681 (2022)
- S. C. Glotzer, M. J. Solomon, Anisotropy of building blocks and their assembly into complex structures. Nat. Mater. 6, 557-562 (2007).
- S. C. Fischer, G. W. Bassel, P. Kollmannsberger, Tissues as networks of cells: Towards generative rules of complex organ development. *J. R. Soc. Interface* **20**, 20230115 (2023).

  X. Wang *et al.*, Anisotropy links cell shapes to tissue flow during convergent extension. *Proc. Natl.*
- Acad. Sci. U.S.A. 117, 13541-13551 (2020).
- $P.\ Liang,\ X.\ Yang,\ Grain\ shape\ evolution\ of\ sand-sized\ sediments\ during\ transport\ from\ mountains$ to dune fields. J. Geophys. Res. Atmos. 128, e2022JF006930 (2023).
- S. Ghadr, A. Assadi-Langroudi, Effect of grain size and shape on undrained behaviour of sands. Int. J. Geosynth. Ground Eng. 5, 18 (2019).
- P. M. Chaikin, T. C. Lubensky, *Principles of Condensed Matter Physics* (Cambridge University Press, 8. ed. 1, 2000).
- A. A. Shah et al., Liquid crystal order in colloidal suspensions of spheroidal particles by direct current electric field assembly. Small 8, 1551-1562 (2012).
- T. G. Anjali, M. G. Basavaraj, Shape-anisotropic colloids at interfaces. Langmuir 35, 3-20
- 11. J. Mewis, N. J. Wagner, Colloidal Suspension Rheology (Cambridge University Press, 2012).
- 12. S. Mueller, E. W. Llewellin, H. M. Mader, The rheology of suspensions of solid particles. Proc. R. Soc. A Math. Phys. Eng. Sci. 466, 1201-1228 (2010).
- C. Ness, R. Seto, R. Mari, The physics of dense suspensions. Annu. Rev. Condens. Matter Phys. 13, 97-117 (2022).
- N. I. Heywood, Stop your slurries from stirring up trouble. Chem. Eng. Prog. 95, 21–40 (1999).
   V. Wenzel, H. Nirschl, D. Nötzel, Challenges in lithium-ion-battery slurry preparation and potential of modifying electrode structures by different mixing processes. Energy Technol. 3, 692-698 (2015)
- 16. J. F. Morris, Toward a fluid mechanics of suspensions. Phys. Rev. Fluids 5, 110519 (2020).
- J. A. Lee et al., Avoiding surface instability and slurry jamming in simultaneous multilayer coating of structured particulate films. J. Coat. Technol. Res. 19, 131–142 (2022).
- B. Zhao, J. Wang, 3d quantitative shape analysis on form, roundness, and compactness with  $\mu$ ct. Powder Technol. 291, 262-275 (2016).
- W. Fei, G. A. Narsilio, M. M. Disfani, Impact of three-dimensional sphericity and roundness on heat transfer in granular materials. Powder Technol. 355, 770-781 (2019).
- M. A. Maroof, A. Mahboubi, A. Noorzad, Y. Safi, A new approach to particle shape classification of granular materials. Transp. Geotech. 22, 100296 (2020).
- 21. G. Batchelor, The stress system in a suspension of force-free particles. J. Fluid Mech. 41, 545-570
- 22. H. Brenner, Rheology of a dilute suspension of axisymmetric brownian particles. Int. J. Multiph. Flow 1, 195-341 (1974).
- 23. G. K. Batchelor, The stress generated in a non-dilute suspension of elongated particles by pure straining motion. J. Fluid Mech. 46, 813-829 (1971).
- 24. C. H. Hsueh, W. C. Wei, Effective viscosity of semidilute suspensions of rigid ellipsoids. J. Appl. Phys. 107, 024905 (2010).
- M. James, H. Xue, M. Goyal, H. M. Jaeger, Controlling shear jamming in dense suspensions via the particle aspect ratio. Soft Matter 15, 3649–3654 (2019).
- 26. M. Mahmoudian, F. Goharpey, M. Behzadnasab, Z. Daneshfar, Shear thickening and hysteresis in dense suspensions: The effect of particle shape. J. Rheol. 68, 479-490 (2024).
- 27. M. Fan, D. Su, X. Chen, Framework for incorporating multi-level morphology of particles in DEM simulations: Independent control of polydisperse distributions of roundness and roughness while preserving form distributions in granular materials. Acta Geotech. 19, 4557-4580 (2024).
- A. Singh, G. L. Jackson, M. van der Naald, J. J. de Pablo, H. M. Jaeger, Stress-activated constraints in dense suspension rheology. Phys. Rev. Fluids 7, 054302 (2022).
- I. R. Peters, S. Majumdar, H. M. Jaeger, Direct observation of dynamic shear jamming in dense suspensions. Nature 532, 214-217 (2016).
- L. C. Hsiao et al., Rheological state diagrams for rough colloids in shear flow. Phys. Rev. Lett. 119,
- 31. S. Pradeep, M. Nabizadeh, A. R. Jacob, S. Jamali, L. C. Hsiao, Jamming distance dictates colloidal shear thickening. Phys. Rev. Lett. 127, 158002 (2021).
- S. Khalid et al., Poly(lactic acid)/starch composites: Effect of microstructure and morphology of starch granules on performance. J. Appl. Polym. Sci. 134, 45504 (2017).
- F. Blanc, E. D'Ambrosio, L. Lobry, F. Peters, E. Lemaire, Universal scaling law in frictional nonbrownian suspensions. Phys. Rev. Fluids 3, 114303 (2018).

- 34. E. Lemaire et al., Rheology of non-brownian suspensions: A rough contact story. Rheol. Acta 62, 253-268 (2023).
- 35. A. Djellouli et al., Shell buckling for programmable metafluids. Nature 628, 545-550 (2024).
- 36. M. Liu, X. Zheng, F. Dong, M. D. Ward, M. Weck, Reversible morphology switching of colloidal particles. Chem. Mater. 30, 6903-6907 (2018).
- 37. N. Tanjeem, M. B. Minnis, R. C. Hayward, C. W. Shields, Shape-changing particles: From materials design and mechanisms to implementation. Adv. Mater. 34, e2105758 (2022).
- 38. M. Warner, E. M. Terentjev, Liquid Crystal Elastomers (Oxford University Press, 2003).
- 39. C. Ohm, M. Brehmer, R. Zentel, Liquid crystalline elastomers as actuators and sensors. Adv. Mater. 22, 3366-3387 (2010).
- 40. T. J. White, D. J. Broer, Programmable and adaptive mechanics with liquid crystal polymer
- A. S. Wille, D. S. Diele, Programmable and adaptive metalarits with riquid crystal polyiner networks and elastomers. *Nat. Mater.* 14, 1087–1098 (2015).
   R. S. Kularatne, H. Kim, J. M. Boothby, T. H. Ware, Liquid crystal elastomer actuators: Synthesis, alignment, and applications. *J. Polym. Sci. Part B Polym. Phys.* 55, 395–411 (2017).
- X. Liu et al., Programmable liquid crystal elastomer microactuators prepared via thiol-ene dispersion polymerization. Soft Matter 16, 4908-4911 (2020).
- C. Ohm et al., Microfluidic synthesis of highly shape-anisotropic particles from liquid crystalline elastomers with defined director field configurations. J. Am. Chem. Soc. 133, 5305-5311 (2011).
- T. D. Nguyen, E. Jankowski, S. C. Glotzer, Self-assembly and reconfigurability of shape-shifting particles. ACS Nano 5, 8892-8903 (2011).
- 45. M. Liu et al., Switching chirality in arrays of shape-reconfigurable spindle microparticles. Adv. Mater. 35, e2303009 (2023).
- 46. M. K. Abdelrahman et al., The role of solvent molecular weight in shear thickening and shear
- jamming. Nat. Mater. 23, 281-289 (2024). 47. M. van der Naald, L. Zhao, G. L. Jackson, H. M. Jaeger, The role of solvent molecular weight in shear
- thickening and shear jamming. Soft Matter 17, 3144-3152 (2021).
- C. Chen et al., Leveraging the polymer glass transition to access thermally switchable shear jamming suspensions. ACS Central Sci. 9, 639–647 (2023).
- 49. A. V. N. Le, A. Izzet, G. Ovarlez, A. Colin, Solvents govern rheology and jamming of polymeric bead suspensions. J. Colloid Interface Sci. 629, 438-450 (2023).
- J. R. Royer, D. L. Blair, S. D. Hudson, Rheological signature of frictional interactions in shear thickening suspensions. Phys. Rev. Lett. 116, 188301 (2016).
- J. Warren et al., Effect of temperature on the shear-thickening behavior of fumed silica suspensions. ACS Appl. Mater. Interfaces 7, 18650-18661 (2015).
- 52. Y. M. Joshi, Dynamics of colloidal glasses and gels. Annu. Rev. Chem. Biomol. Eng. 5, 181-202 (2014).
- 53. L. C. Hsiao, R. S. Newman, S. C. Glotzer, M. J. Solomon, Role of isostaticity and load-bearing microstructure in the elasticity of yielded colloidal gels. Proc. Natl. Acad. Sci. U.S.A. 109, 16029-16034 (2012).
- 54. H. J. Farre-Kaga, M. O. Saed, E. M. Terentjev, Dynamic pressure sensitive adhesion in nematic phase of liquid crystal elastomers. Adv. Funct. Mater. 32, 2110190 (2021).
- T. Ohzono, M. O. Saed, E. M. Terentjev, Enhanced dynamic adhesion in nematic liquid crystal elastomers. Adv. Mater. 31, e1902642 (2019).
- 56. A. Donev, R. Connelly, F. H. Stillinger, S. Torquato, Underconstrained jammed packings of nonspherical hard particles: Ellipses and ellipsoids. Phys. Rev. E Stat. Nonlinear Soft Matter Phys. **75**. 051304 (2007).
- K. W. Lim, K. Krabbenhoft, J. E. Andrade, On the contact treatment of non-convex particles in the granular element method. Comput. Particle Mech. 1, 257–275 (2014).
- M. O. Saed et al., High strain actuation liquid crystal elastomers via modulation of mesophase structure. Soft Matter 13, 7537-7547 (2017).
- Z. S. Davidson et al., Monolithic shape-programmable dielectric liquid crystal elastomer actuators. Sci. Adv. 5, eaay0855 (2019).
- R. P. Murphy, K. Hong, N. J. Wagner, Thermoreversible gels composed of colloidal silica rods with short-range attractions. Langmuir 32, 8424-8435 (2016).
- Y. Jiang, S. Makino, J. R. Royer, W. C. Poon, Flow-switched bistability in a colloidal gel with nonbrownian grains. Phys. Rev. Lett. 128, 248002 (2022).
- 62. A. Hodaei et al., Single additive enables 3d printing of highly loaded iron oxide suspensions. ACS Appl. Mate. Interfaces 10, 9873-9881 (2018).
- 63. A. Krishnaraja, K. Guru, 3d printing concrete: A review. IOP Conf. Ser. Mater. Sci. Eng. 1055, 012033 (2021).
- C. A. Schneider, W. S. Rasband, K. W. Eliceiri, NIH Image to ImageJ: 25 years of image analysis. Nat. Methods 9, 671-675 (2012).
- 65. J. Schindelin et al., Fiji: An open-source platform for biological-image analysis. Nat. Methods 9, 676-682 (2012).